Translational spectroscopy of metastable fragments produced by dissociative excitation of atmospheric gases by electron impact. I. Nitrogen*

W. C. Wells

Lockheed Palo Alto Research Laboratory,† Lockheed Missiles and Space Company, Palo Alto, California 94304 and Department of Physics, University of Pittsburgh, Pittsburgh, Pennsylvania 15260

W. L. Borst‡ and E. C. Zipf

Department of Physics, University of Pittsburgh, Pittsburgh, Pennsylvania 15260

(Received 2 September 1975; revised manuscript received 15 December 1975)

Kinetic-energy spectra of long-lived high-Rydberg nitrogen atoms produced by electron impact dissociative excitation were measured using a time-of-flight apparatus. Four principal features were found in the fragment kinetic-energy spectra with peaks at 0.6, 2.4, 3.4, and 6.7 eV. The excitation function exhibited a sharp resonance-like behavior near a threshold of 24.1 eV, corresponding to fragment production of $N(^4S) + N^{**}$, where N^{**} is a high-Rydberg atom with an energy near the ionization limit of N(14.54 eV). The observed features are discussed in terms of the core-ion model of high-Rydberg dissociation. The data are compared with other dissociative excitation and dissociative ionization work. The maximum differential cross section for the production of energetic long-lived high-Rydberg N atoms was found to be $d\sigma/d\Omega \simeq 9 \times 10^{-20}$ cm^{2}sr^{-1} within a factor of 2 at an electron energy of 180 eV and at an angle of 90° with respect to the electron beam. Geophysical implications of these measurements concerning heating of the atmosphere, radiative transfer of resonance radiation, and chemical reactions are mentioned briefly.

I. INTRODUCTION

Translational spectroscopy is a powerful tool whereby the nature of molecular structure can be discerned by measuring the velocity and kinetic-energy spectra of dissociation fragments in time-of-flight (TOF) experiments.[1] Previous reports[2-5] of this work have been brief and concentrated only on the most salient features. Dissociation of atmospheric gases by electron impact is an important atmospheric collision. In addition, metastable species play an important role in the ionization balance and thermal economy of planetary atmospheres and are responsible for a significant amount of radiation in airglow and auroral phenomenon. Taken together, the electron-impact dissociative excitation of metastable species is a significant process whose aeronomical implications have yet to be fully considered. These processes can also be important in the chemistry of lasers.[6]

In this paper we report the dissociative excitation of metastable nitrogen atoms produced by electron impact on N_2.[7] Dissociation of molecular nitrogen is of particular interest, since metastable nitrogen atoms play a dominant role in Earth's atmosphere. In this experiment our detector threshold (~5 eV) restricted us to the study of high-lying metastable states of the N atom including high-lying long-lived Rydberg atoms.[8]

The production of fast highly excited nitrogen atoms was observed from threshold to 300 eV. Processes were observed with peaks in the kinetic energies at 0.6, 2.4, 3.4, and 6.7 eV, and atoms with as much energy as 25 eV at higher electron-impact energies. Excitation functions peaked in the 40–250-eV region with the maximum being correlated with the kinetic energy of the atoms.

II. DISSOCIATION PROCESS

Electron impact on a molecule can result in a vertical transition from the ground state to a repulsive state which subsequently decays with one or more excited fragments flying apart (Fig. 1). Dissociative excitation may also result from excitation of a bound electronic state which predissociates. In our discussion here we will consider the case of the diatomic molecule, but the arguments apply to larger molecules as well. When the excited fragment atom is a high-Rydberg atom we can describe the process with the ion-core model.

A. Ion-core model

The ion-core model, first suggest by Kupriyanov,[9] has been used to explain the dissociative excitation of high-lying Rydberg states[4,10-13] and has been discussed at length by Freund[10] and Smyth *et al.*[11] We give a cursory description of the ion-core model here. The reader is referred to Refs. 10 and 11 for more extensive discussions. In this model the ground-state electron is excited to a high level in a Rydberg series which converges to one of the ionization limits of the mo-

lecule, leaving the core ion in a repulsive state. The high-lying Rydberg electron can be treated as a "spectator" orbiting the molecule at such large distances (hundreds of angstroms) that it leaves the "core" ion relatively unperturbed. Hence, it is the repulsive states of the molecular ion which determine the dissociation processes and products. When the molecular core ion dissociates into a neutral atom and ion, the ion picks up the orbiting molecular Rydberg electron and leaves it in a corresponding high-Rydberg atomic orbital. Therefore, we would expect great similarities in the dissociative excitation of high-Rydberg atoms and in dissociative ionization as far as kinetic-energy spectra and excitation functions are concerned. This is in fact the case.[4,10-13]

High-Rydberg states are characterized by lifetimes which vary as n^3 with respect to radiation[14] and autoionization.[15] Lifetimes of Rydberg atoms observed in this experiment are greater than about 10 μsec which indicates that the likely n values fall in the range of 50–300.

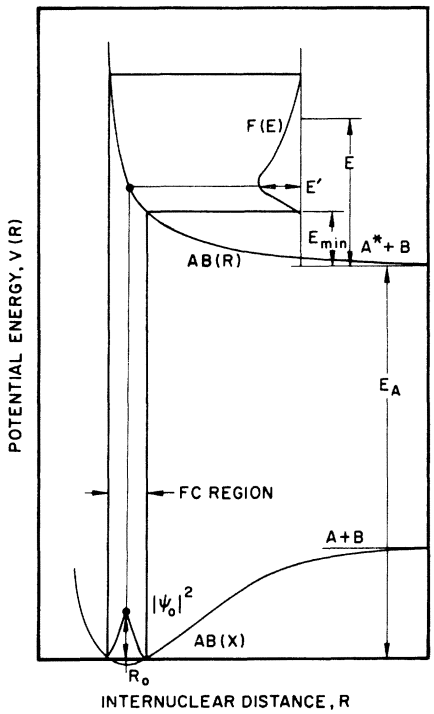

FIG. 1. Potential-energy diagram for the diatomic molecule AB. Electron-impact excitation takes place from the $v=0$ level of the ground state X vertically to the dissociative state R. The molecule dissociates leaving fragment A excited, giving the fragments a total-kinetic-energy spectrum of $F(E)$. Dissociation from a purely repulsive curve leads to a zero value of the energy spectrum at a finite kinetic energy E_{min}. Construction of the potential curve in the Franck-Condon region from the total-kinetic-energy spectra and the probability distribution $|\psi_0|^2$ is shown and is described in the text.

B. Kinetic-energy spectra

In our experiment we measure the time-of-flight spectrum $T(t)$ of an excited fragment A^* as a function of electron-impact energy. To derive the kinetic-energy spectrum $D(\epsilon)$, consider that the kinetic energy ϵ of A^* is inversely proportional to the square of the arrival time t, so that

$$|d\epsilon| \propto t^{-3}|dt|. \tag{1}$$

Then, $T(t)dt$, the number of excited atoms arriving at the detector between time t and $t+dt$, can be expressed as

$$T_A(t)|dt| = T_A(t)t^3|d\epsilon|, \tag{2}$$

ignoring a constant factor. Thus, the kinetic-energy spectrum is given by

$$D_A(\epsilon_A) = t^3 T_A(t). \tag{3}$$

From conservation of momentum the kinetic-energy relationship between fragments A and B with masses m_A and m_B is

$$\epsilon_B = (m_A/m_B)\epsilon_A. \tag{4}$$

Thus, it follows that the kinetic-energy spectrum for fragment B, $D_B(\epsilon_B)$, is

$$D_B(\epsilon_B) = D_A \frac{m_B}{m_A}\epsilon_B, \tag{5}$$

and the total-released-kinetic-energy spectrum $F(E)$ is

$$F(E) = D_A\left(\frac{m_B}{m_A+m_B}E\right),$$

where $E = \epsilon_A + \epsilon_B$. We have neglected the thermal energy of the molecule in this treatment (see Sec. IIID).

C. Repulsive-potential-energy curves

As can be seen in Fig. 1, the spectrum of the total released kinetic energy, $F(E)$, in a dissociation process is determined by the nature of the repulsive-energy curve in the Franck-Condon region. Conversely given the total released kinetic energy spectrum, it is possible to construct the potential energy curve in the Franck-Condon region. We assume here that the wave function for the repulsive state can be closely approximated by a δ function[16] and that the Franck-Condon principle holds near threshold. The value of the asymptotic limit E_A of the potential curve is the excitation-function threshold less the minimum kinetic energy E_{min}.

The mathematical prescription for the construction of the repulsive curve from the ground-state probability function $|\psi_0|^2$ and the total-released-kinetic-energy spectra $F(E)$ [both normalized to a maximum height of 1, $|\psi_0(R_0)|^2 = F(E) = 1$ follows.

When the probability function

$$|\psi_0(R_{1,2})|^2 = \exp[-\alpha(R_{1,2} - R_0)^2] \tag{6}$$

is equal to the energy-spectra function $F(E_{1,2})$, then

$$V(R_{1,2}) = E_A + E_{1,2}, \tag{7}$$

where R is the internuclear distance, V the potential energy, and E the total kinetic energy released. It is assumed here that the vibrational motion of the molecule can be described as a harmonic oscillator and that the molecule is in its ground vibrational state. Equation (7) is satisfied for two values of R, R_1 and R_2, thus giving two points on curve V, $V(R_1)$ and $V(R_2)$. Equation (7) can be inverted to yield

$$R(V) = \begin{cases} R_0 + \left| \left(\dfrac{\ln F(V - E_A)}{-\alpha} \right)^{1/2} \right|, & V < V(R_0) = E_A + E, \\ R_0 - \left| \left(\dfrac{\ln F(V - E_A)}{-\alpha} \right)^{1/2} \right|, & V > V(R_0), \end{cases} \tag{8}$$

which is the analytical representation of this numerical process.

III. EXPERIMENTAL APPARATUS

A schematic diagram of the TOF apparatus used in these experiments is shown in Fig. 2. The basic elements included a periodically pulsed system for metastable production, a metastable detector, and a digital processing system. Details of these systems are described below.

The metastable production and detection systems were housed in an ultrahigh-vacuum chamber. Gas was admitted into the collision chamber by means of a gas-handling system incorporating an automatic pressure controller. The gas pressure was about 10^{-4} Torr and approximately uniform within the collision chamber. (The background pressure was about 1×10^{-7} Torr.) Under these conditions the collision chamber closely approximated a diffuse-gas source.

A. Metastable production

Metastable fragments were produced by electron impact in the energy range from threshold to about 300 eV. The electron gun used in these experiments was similar to a gun described previously.[17] Because of the required relatively high beam current (1 μA) and good energy resolution [0.3 eV full width at half-maximum (FWHM)], the gun was not operated in the retarding-potential-difference (RPD) mode. A magnetic field of about 150 G collimated the electron beam. The electron gun was pulsed at the retarding plate to inject bursts of electrons into the collision chamber. This enabled one to measure the arrival time of the metastable fragments at the detector, and thus we obtained time-of-flight distributions. Beam pulses were typically 0.5 μsec wide with repetition rates of about 10^3 pulses/sec. The duty cycle of the gun was thus about 0.05%. The equipment for pulsing the gun consisted of a time-mark generator, discriminator, gate generator, and beam pulser; these are shown in Fig. 2.

B. Metastable detection

After collimation and charge-particle removal, metastable fragments were detected at an angle of 90° with respect to the beam direction when they impinged upon the first dynode of a nude Cu-Be electron multiplier thereby liberating secondary electrons via the Auger process.[18] Thus, the detector was sensitive to all those metastable fragments with excitation energies in excess of the work function of the multiplier dynodes ($\phi \sim 5$ eV).

The solid angle subtended by the multiplier

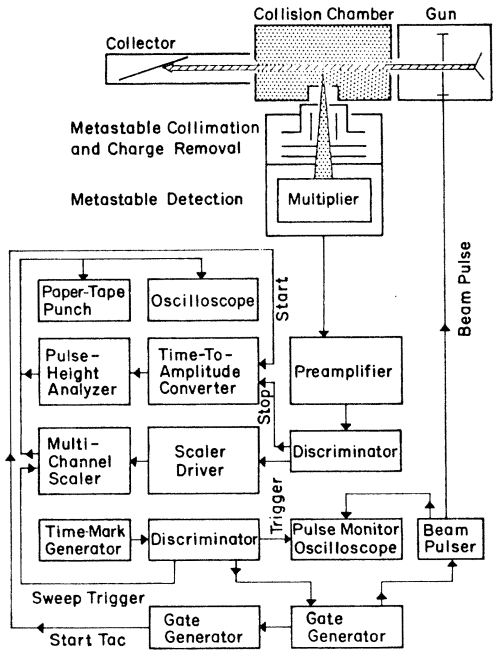

FIG. 2. Schematic diagram of the experimental apparatus used to make time-of-flight distributions. For the observations reported here the time-to-amplitude converter and the pulse-height analyzer were used.

entrance aperture was about 0.05 sr. The effective scattering length in the collision chamber was about 0.5 cm. The distance between the center of the collision chamber and the first dynode of the Cu-Be electron multiplier was 6.4 cm. This resulted in transit times for metastable fragments of anywhere from 3–50 μsec (see Fig. 3).

Total counting rates at the detector, summing over all metastable-fragment arrival times, were of the order of 10–100 counts/sec. The background counting rate was about 0.05 counts/sec. The low signal levels encountered clearly indicated the advantage of multiscaling techniques in order to obtain good time resolution as well as good statistics in the time-of-flight spectra.

C. Data processing

Time-of-flight spectra of metastable fragments were obtained with a multichannel-analyzer system (Fig. 2) operated either in a pulse-height-analyzer (PHA) mode with a time-to-amplitude (TAC) converter or in a multichannel-scaler (MCS) mode for longer arrival times. Most of the work on N_2 was done with the PHA and TAC. Time calibration was carried out using pulse generators with crystal controlled time bases. The accumulation time for each TOF distribution (Fig. 3) was about 2 h. This corresponded to about 10^7 beam pulses. The time spacing between pulses was 1 msec to allow the Maxwell-Boltzmann tail on the thermal metastable nitrogen molecules to decay.[19]

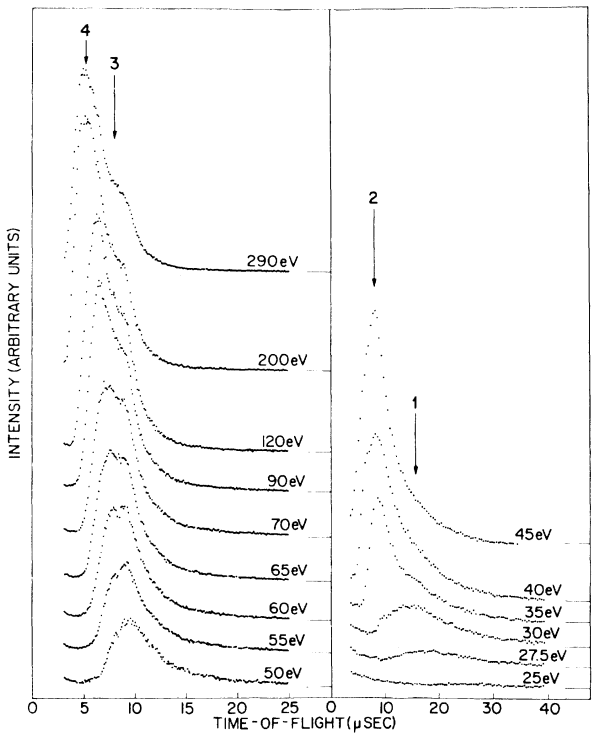

FIG. 3. Time-of-flight distributions for long-lived high-Rydberg nitrogen atoms. Discernible features are grouped into four groups and numbered. The right side shows the relative slow fragments for electron impact energies between 25 and 45 eV while the left side shows the faster fragments at higher energies. Each set of data is plotted with relative ordinates.

Excitation functions (see Fig. 5) were obtained with a delayed coincidence network which was composed of a single-channel analyzer of variable channel width and position. Its components consisted of gate generators for window position and width, a coincidence unit, a counter, and a dual-beam oscilloscope. The multichannel scalar (MCS) was used as a signal averager where its ramp voltage was used to drive the programmable electron-beam energy power supply. The beam energy was swept from zero to its maximum value every 30 sec with a sawtooth ramp. Before and after an excitation-function run, which took anywhere from 2 to 30 h, the beam current and the beam energy were recorded as a function of channel number using a voltage-to-frequency-converter (VCO) to convert the dc voltages to a pulse train, the repetition rate of which was proportional to the voltage. The excitation functions were current normalized by dividing by the beam current channel by channel. No discernible drifts were found in the energy dependence of the beam current or the energy calibration of the signal averager. The magnitude of the beam current was noticed to drift slowly by as much as 50% over a period of a long run. This translated to less than a 0.5% distortion of the excitation function, which was less than our statistical noise and was neglected. This example is a good illustration how signal averaging is not susceptible to relatively large long term experimental drifts. Signal averaging gave us much better statistics than attainable before[20] and enabled us to better define thresholds as a function of small TOF windows. The energy scale was calibrated absolutely by observing the threshold for He($2\,^3S$) at 19.8 eV.

D. Experimental uncertainties

1. Thermal-energy spread

The effect of the thermal motion of the target molecule is to add or subtract a velocity component v_{th} from the velocity of the fragment v_f. In terms of a center-of-mass coordinate transformation, the situation can be viewed with the fragment having a velocity v_f in the center-of-mass system, which itself is moving with velocities

between $\pm v_{th}$ with respect to the lab system. The resultant velocity spread in the lab system results in a fragment energy spread given by

$$\Delta E_f = 2[2E_f E_{th}]^{1/2}, \quad (9)$$

where E_f is the fragment energy and E_{th} is the thermal energy of the parent molecule. For a diffuse N_2 source at 300 °K we have

$$\Delta E_f = 0.45E_f^{1/2}. \quad (10)$$

For a fragment kinetic energy of 5 eV this corresponds to a spread of 1 eV.

2. *Recoil effect*

Momentum recoil arises from the kick the electron gives the molecule when exciting it above threshold. For heavier molecules like N_2 this is not a serious effect. For a 5-eV fragment and an excess electron energy of 20 eV we would have a spread in fragment energy of 0.1 eV.

3. *Beam pulse width*

The beam pulse width introduced a spread in E_f given by

$$\Delta E_f = 2E_f \Delta t/t, \quad (11)$$

where Δt is the beam pulse width and t the arrival time at the detector. For the 0.5-μsec pulse width used here and a 5-eV fragment, the spread corresponded to $\Delta E_f \sim 1$ eV. This error manifests itself as a distortion in the high-energy part of the kinetic-energy distribution and as an ambiguity in time-of-flight windows associated with short arrival times, e.g., excitation functions for fast fragments.

In this experiment the beam pulse shape was a square wave up to energies of about 270 eV. Above 270 eV the beam pulse had a Gaussian shape with a full width at half-maximum of about 1 μsec. This resulted in distortion of the 290-eV TOF curve.

4. *Time calibration*

The zero time was established by using the center of the photon pulse. This introduced a possible offset error of less than 0.1 μsec due primarily to the large metastable tail on the photon pulse. This would correspond to a systematic error of 0.2 eV in the example above.

5. *Charged-particle rejection*

It was observed in our preliminary work at energies less than 50 eV that charged particles were not seen. It was argued that because of the magnetic field and space charge in the collision region, ions could not escape. Subsequent to these observations the charge deflection plates were removed and charge removal was accomplished by alternately biasing the collimation rings on the detector housing with positive and negative voltages. At this point in time positively and negatively charged particles could be detected depending on how the bias potentials were set. These observations will be the subject of a future publication. For the work reported here, the potentials were adjusted so as to reject any charged-particle contributions. It could be argued that this technique of charge removal is inferior to the use of deflection plates and some ions could leak through. Careful examination of our data gave no evidence of this happening.

6. *Asymptotic appearance potentials*

In Fig. 6 observed appearance potentials (Fig. 5) are plotted against the total released kinetic energy. The total released kinetic energy is taken as twice the lower limit of the fragment kinetic energy seen by the respective excitation function. If in fact the minimum fragment kinetic energy for a given process falls within the range for a given excitation function rather than below, then an error is introduced. This could only possibly happen for the first point in a series, where the error would be evidenced by the point lying above the line. This was not observed to be a problem in our data when two or more points were involved in the extrapolation. A definite uncertainty is introduced for those features where the extrapolated appearance potential is determined by one point. This uncertainty is related to the difference in the minimum fragment kinetic energy for the process and the lower limit of the excitation-function window. This was the case for the highest two of the nine appearance potentials observed.

IV. EXPERIMENTAL RESULTS

A. TOF results and kinetic-energy spectra

Time-of-flight data are presented in Fig. 3. At short arrival times a photon signal is visible as an exponential tail. Its source is discussed below. Transforming the TOF spectra using Eq. (3) gave fragment kinetic-energy spectra which are shown in Fig. 4. At low electron impact energies feature 1 is clearly visible with a peak energy of about 0.6 eV. At higher energies (~ 35 eV) feature 2 is visible with a peak around 2.4 eV. At still higher energies (~ 55 eV) feature 3 dominates the spectra with a peak around 3.4 eV. In the energy range 60–300 eV feature 4 is seen growing with a peak around 6.7 eV and a maximum kinetic ener-

gy in excess of 25 eV. A shoulder is discernible for feature 4 at about 5 eV. Features 2–4 probably correspond to several processes which are not resolved in the TOF data.

B. Excitation functions

Excitation functions are shown in Fig. 5 for different fragment kinetic-energy intervals. Thresholds for the various features were established by using straight-line segments to fit the excitation functions. For features 2 and 4 this introduces some uncertainty since the statistics were not good enough to uniquely determine a straight-line-segment fit to the data over against a curved-line fit.

In a preliminary report[5] of this work, feature 2 was described with a single threshold. Further examination of the data suggested in fact that three breaks in the excitation function could be found in the region of feature 2. But owing to the poor statistics we would consider this interpretation of the data as suggestive rather than definitive.

The observed threshold from Fig. 5 are plotted in Fig. 6 as a function of the total released kinetic energy in the dissociation process. This is taken to be twice the minimum kinetic energy of the individual fragments. For processes with the same dissociation limit, the points should fall on a straight line of unit slope. The observed thresholds are also tabulated in Table I along with the appearance potentials corresponding to the zero-kinetic-energy intercept.

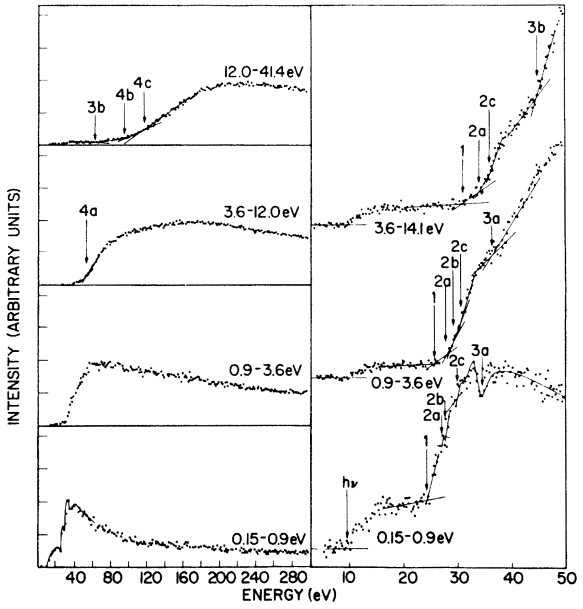

FIG. 5. Time-resolved excitation functions for dissociative excitation of high-Rydberg nitrogen atoms. The fragment kinetic-energy interval is noted next to the excitation function. The thresholds for the same feature shift by the difference in the total released minimum kinetic energies from one excitation function to the next.

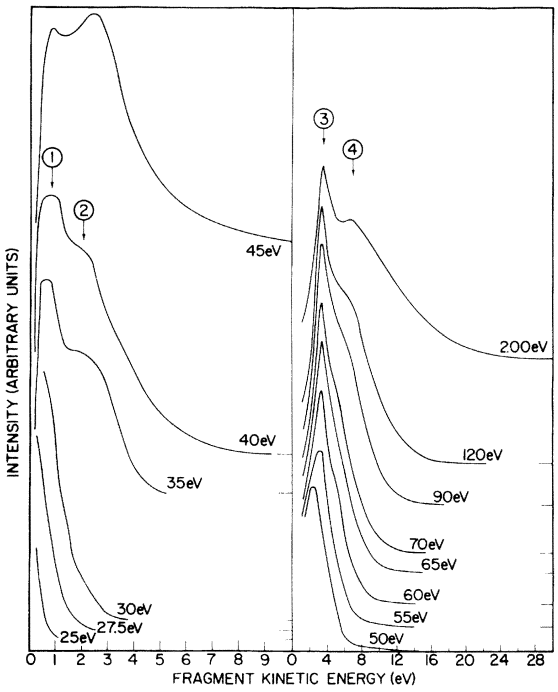

FIG. 4. Kinetic-energy spectra of the high-Rydberg nitrogen atoms obtained from the time-of-flight distributions in Fig. 3. Peaks are seen for the four features at 0.6, 2.4, 3.4, and 6.7 eV.

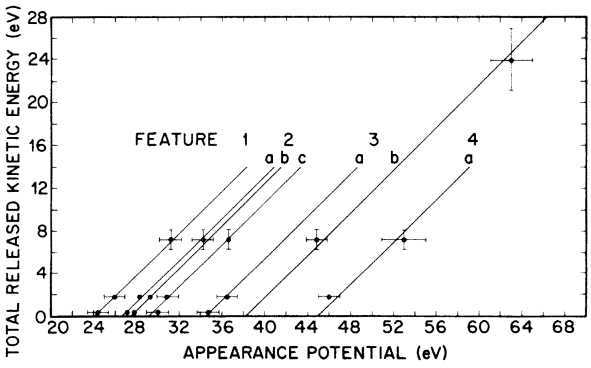

FIG. 6. Plots of total released minimum kinetic energies versus observed appearance potentials. Points have been fitted with a line of unit slope to yield the asymptotic appearance potential corresponding to zero kinetic energy released. Vertical error bars are a measure of the kinetic-energy spread and horizontal error bars are a measure of the uncertainty in the determination of the appearance potential.

TABLE I. Observed appearance potentials. (Units are in eV.)

Total released kinetic energy (eV)	Feature 1	2a	2b	2c	3a	3b	4a	4b	4c
0.3	24.4 [a]	27.1	27.8	30.0	34.7				
1.8	26.0	28.2	29.3	30.9	36.5		46		
7.2	31.2	34.2		36.6		44.8	53 ±2		
24						63 ±2		95±4	118±4
Asymptotic appearance potential (kinetic energy = 0)	24.1	26.7	27.5	29.4	34.6	38.3±2	45.0±2	71±4	94±4

[a] Uncertainty unless noted otherwise is ±1 eV.

C. uv photons

Photons with $\lambda < \sim 2500$ Å were observed in our experiment and are evidenced by an exponential-like decay from the beam pulse in the TOF plots (Fig. 3) and by low-energy pedestals in the excitation-function plots (Fig. 5). Onset was at 9.8 eV, as can be seen in the 0.15–0.9-eV plot (Fig. 5), which corresponded to a TOF window of 18.2–45 μsec. We identified the observed onset and shape of the photon excitation function with the LBH emission from N_2. Above 14 eV there are additional photon contributions from higher-lying long-lived states in N_2.

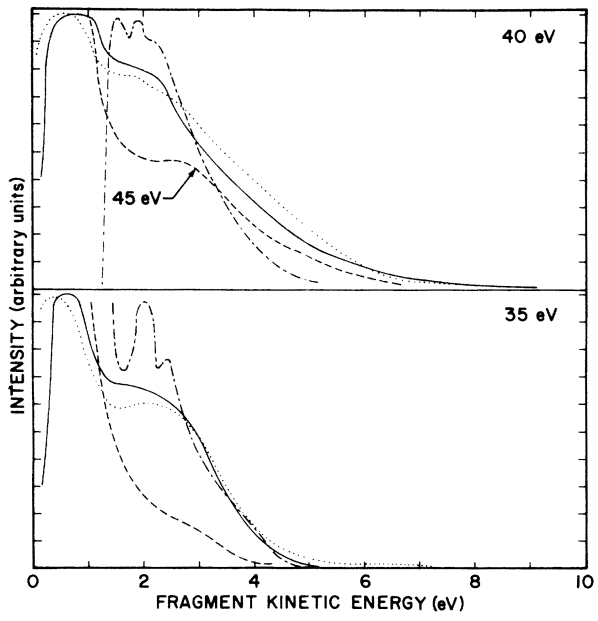

FIG. 7. Comparison of fragment kinetic-energy spectra for high-Rydberg fragments (solid line, this work; dotted line, Smyth *et al.*, Ref. 11) and for N^+ ion fragments (dash-dot line, Deleanu and Stockdale, Ref. 23; dashed line, Tate and Lozier, Ref. 23). All data were taken at an angle of 90°. High-Rydberg data were normalized to each other at their maximum. N^+-ion data were normalized to the high-Rydberg data in the 1–2-eV region to permit comparison of the high-energy features. Electron-impact energies are noted.

D. Cross sections

Estimates of the absolute cross sections for the excitation functions in Fig. 5 were made. The counting rate C corresponding to a TOF interval between t and $t+\Delta t$ observed at the detector is given by

$$C_t = \frac{I_b}{e} nl\Delta\Omega \sum_i \left[\frac{d\sigma_i}{d\Omega}\right]_t \gamma_i \exp(-t/\tau_i), \qquad (12)$$

where I_b is the beam current, e the electronic charge, n the N_2 density, l the effective scattering length of the collision chamber, and $\Delta\Omega$ the solid angle subtended by the detector at the center of the collision chamber. The differential cross section at an angle of 90° with respect to the electron beam for production of N atoms in the ith state, N(i), with arrival times between t and $t+\Delta t$ is $[d\sigma_i/d\Omega]_t$. The secondary yield for N(i) atoms incident on CuBe and the inflight decay lifetime for N(i) atoms are given by γ_i and τ_i, respectively.

Not knowing the radiative lifetimes we have neglected them here. We feel this is justified as the lifetimes appear to be of the order of 100 μsec or longer, based on the similarity of the TOF curves in Fig. 3 to our earlier work,[4] where the TOF distance was three times that used here. Furthermore, it was assumed that all the excited atoms detected had an energy within 0.1 eV of 14.53 eV, the ionization limit for N. The secondary yield for this energy was taken[21] as $\gamma \sim 0.08$.

The differential cross sections are listed in Table II for selected fragment kinetic-energy intervals and are accurate to within a factor of 2, the major uncertainty being in γ. If we assume that the angular distribution is approximately isotropic as is the case for dissociative ionization,[22,23] then an estimate of the maximum total cross section for high-Rydberg production would be $\sigma \sim 10^{-18}$ cm^2 at 180 eV.

TABLE II. Differential cross sections for production of high-Rydberg N atoms.

Fragment kinetic-energy range (eV)	$\left[\left(\frac{d\sigma}{d\Omega}\right)_{90°}\right]_{max}$ ($cm^2 sr^{-1}$)	Electron-beam energy (eV)
0.15–0.9	4.6×10^{-21}	35
0.9–3.6	1.9×10^{-20}	70
3.6–12.0	5.5×10^{-20}	165
12.0–41.4	1.9×10^{-20}	225
Total	9.1×10^{-20}	180

V. DISCUSSION

A. Dissociation processes

Table III lists some dissociation processes for N_2 and expected energy thresholds. The appearance potentials for our work are listed for comparison purposes. Feature 1 corresponds to the ion analog for dissociative ionization yielding $N^+(^3P)+N(^4S)$. Feature 2 is more complex. Features 2a and 2b may correspond to the high-Rydberg production with the other fragment being $N(^2D)$ and $N(^2P)$, respectively. This would be consistent with work done on dissociative ionization. Features 2c and 4a may correspond to $N(^6S_{5/2})$ production and are discussed separately below.

Feature 3a corresponds to the other fragment being in the first Rydberg state of the atom, $N(3s\,^4P)$. The cross section for the simultaneous dissociative ionization and excitation of $N(3s\,^4P)$ corresponds well with the excitation function of Smyth *et al.*[11] for the production of feature 3a. At higher kinetic energies, feature 3b is seen and corresponds to the ion analog of simultaneous ionization, $N^+(^3P)+N^+(^3P)$. Smyth *et al.*[11] observed that between the appearance potentials for features 3a and 3b they were seeing other processes corresponding to the other fragment coming off in a Rydberg state between $N(3s\,^4P)$ and the ion limit $N^+(^3P)$. Our work would tend to confirm this observation.

It is difficult to uniquely identify processes with thresholds above 45 eV that might account for the very fast fragments which we have labeled feature 4. Very likely there are a host of processes which contribute in the energy range 50–200 eV, where feature 4 is seen to grow (Fig. 4).

Features 4b and 4c may correspond to the other fragment being N^{2+} in the ground state or the $2p^3\,^4S^o$ state. Note that the difference in appearance potentials for processes 9 and 10 is in excellent agreement with what we observe even though the absolute energies differ by about 2.5 eV. Nonetheless processes 9 and 10 may not be observable in our data after all if the excitation function for 12 eV and faster fragments, which we fitted with straight-line segments, is in fact curved at threshold.

At these higher energies where multielectron processes are involved, larger amounts of kinetic energy are imparted to the fragments. This fact may shed some light on just how the processes

TABLE III. Selected dissociation processes for N_2.

Process	Dissociation fragments	Predicted appearance potentials (eV)	Feature	This work (eV)
1	$N(^4S)+N^{**}$	24.29 [a]	1	24.1 [b]
2	$N(^2D)+N^{**}$	26.68	2*a*	26.7
3	$N(^4S)+N(^6S_{5/2})$	27.1 [c]		
4	$N(^2P)+N^{**}$	27.87	2*b*	27.5
5	$N(^2D)+N(^6S_{5/2})$	29.4 [c]	2*c*	29.4
6	$N(3s\,^4P)+N^{**}$	34.62	3*a*	34.6
7	$N^+(^3P)+N^{**}$	38.83	3*b*	38.3±2
8	$N^+(^1D)+N(^6S_{5/2})$	43.4 [c]	4*a*	45.0±2
9	$N^{2+}(^2P)+N^{**}$	68.43	4*b*	71 ±4
10	$N^{2+}(^2p^3\,^4S^o)$	91.59	4*c*	94 ±4

[a] Energy specified is for the ion analog process where the high-Rydberg atom N** is replaced by $N^+(^3P)$.

[b] Uncertainties are ±1 eV unless otherwise specified.

[c] Energy of $N(^6S_{5/2})$ is taken as 17.2 eV (see text).

which make up feature 4 are produced and the connection if any to a multiply ionized core model.

B. $N(^6S_{5/2})$

Fairchild *et al.*[24] in a similar experiment observed long-lived excited fragments which behaved like metastable atoms rather than high-Rydbergs in a quenching field. They suggested that atoms in the metastable autoionizing $2s(2p)^3 3s\ ^6S_{5/2}$ state were being produced in addition to high-Rydberg atoms. The $^6S_{5/2}$ state has never been observed *per se* but its existence has been invoked[25,26] to explain the so-called pink afterglow of nitrogen observed in auroras and flow-tube experiments. Prag and Clark[26] inferred an energy for the $^6S_{5/2}$ state of 17.2 eV based on isolelectronic extrapolation. The actual energy might vary from this value.

The quenching experiments indicated that most of the metastable atoms were fast, corresponding to our feature 4. A subsequent lifetime measurement[27] on some of the slower fragments believed to be $N(^6S_{5/2})$ and corresponding to our feature 2 yielded $\tau = 87 \pm 10$ μsec.

Production of $N(^6S_{5/2})$ atoms should be identifiable in our data as appearance potentials that do not correspond to high-Rydberg processes. Features 2c and 4a with appearance potentials at 29.4 and 45.0 eV are not readily associated with high-Rydberg processes (see Table III). Predicted appearance potentials for $N(^6S_{5/2})$ production with the other fragment in the first excited state of the atom or ion suggest that these are possible candidate processes for features 2c and 4a. It is also possible that process 3 with $N(^4S) + N(^6S_{5/2})$ might correspond to features 2a or 2b. It is difficult to prove or disprove the existence of the $^6S_{5/2}$ with our data owing to the uncertainty in the energy of the state and our poor statistics for feature 2. Nonetheless, $N(^6S_{5/2})$ should not be discarded as a possible dissociation fragment. Work is presently underway to reexamine our TOF and excitation-function results with a quenching field in operation to permit unfolding of the metastable and high-Rydberg contributions.

C. Other work

In Figs. 7 and 8 we compare our kinetic-energy spectra with other work for high-Rydberg and ion fragments. Our work compares well with that of Smyth *et al.*[11] done at a longer distance with a different detector, and with a molecular-beam source. Their time-of-flight path was an order of magnitude longer than ours and their high-Rydberg detector was insensitive to metastable atoms lying below the ionization limit. Our experiment was thus less sensitive to inflight decay of excited atoms. This means that we would have detected relatively more of those atoms with short lifetimes than did Smyth *et al.*[11] If excited atoms with energies greater than the ionization limit of N were detected, their detection efficiencies would have varied in our experiment and been relatively constant in the experiment of Smyth *et al.*[11] This follows from the different responsivities of the two types of detectors. The sensitivity of the Auger detector used in this experiment increases monotonically with increasing excitation energy of the incident fragments while the sensitivity of the field-ionization high-Rydberg detector remains relatively constant.

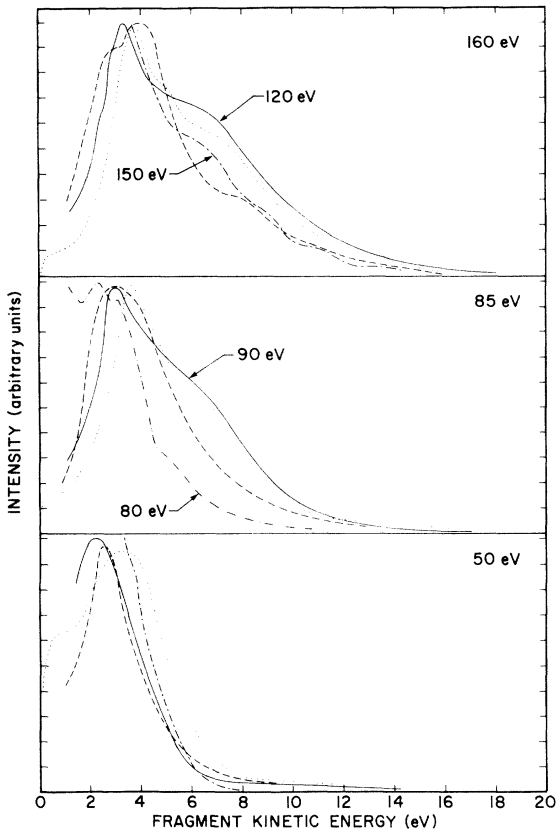

FIG. 8. Comparison of fragment kinetic-energy spectra for high-Rydberg fragments (solid line, this work; dotted line, Smyth *et al.*, Ref. 11) and for N^+ ion fragments (dash-dot line, Deleanu and Stockdale; dashed line, Kieffer and Van Brunt; and dash–double-dot line, Locht Schopman—all Ref. 23). All data were taken at an angle of 90° with the exception of Kieffer and Van Brunt (55°). The data were approximately normalized to each other in the 3–4-eV region. Electron-impact energies are noted in the upper right-hand corner. Data taken at energies differing from the other data are so indicated. More recent data from Kieffer and Van Brunt (Ref. 30) at 50 eV exhibit a shoulder around 1 eV.

TABLE IV. Comparison of appearance potentials and peak fragment kinetic energies (all energies in eV).

Feature	1	2	3	4
Appearance potential				
Smyth *et al.*[a]	24.0	26.4	34.3[b]	•••
This work	24.1	26.7, 27.5 29.4	34.6, 38.3	45, 71, 94
Kinetic-energy peak				
Smyth *et al.*[a]	0.15	2–3	3.65	7.5
This work	0.6	2.4	3.4	5[c], 6.7

[a] Reference 11.
[b] Many appearance potentials observed extending upward to the ion limit at 38.8 eV.
[c] Seen as a weak shoulder.

The minor disparities may be due to differences in the detector sensitivities and the different lifetimes of the excited fragments. Comparison of observed appearance potentials and peak fragment kinetic energies is made in Table IV. Again, agreement is generally good. The discrepancy for the kinetic-energy peak for feature 1 may be due to the difficulty in our experiment of observing fragments at long arrival times owing to the overlapping metastable nitrogen molecules.[19] In addition, because of the t^3 dependence in the transformation to the kinetic-energy distribution discussed in Sec. II B, small errors in background subtraction can be greatly magnified, distorting the distributions for slow fragments. The peaks for features 3 and 4 occur at about 10% less energy in our work. This could be due again to lifetime effects or a small systematic offset in the time scale. In our experiment this would only have to be 0.2 μsec. But even this small error does not seem likely as discussed in Sec. III D.

If the ion-core model is a valid description for high-Rydberg processes we would expect to see similarities in kinetic-energy spectra and cross sections with dissociative ionization processes.[10] In comparing our high-Rydberg kinetic-energy spectra and those of Smyth *et al.*[11] with kinetic-energy spectra[23] for dissociative ionization (see Figs. 7 and 8) we see in general good qualitative agreement. Individual kinetic-energy peaks can be identified with each other. At low energies discrepancies can be accounted for by the insensitivity of the ion experiment to low-energy ions. We must postpone making any qualitative comparisons at low ion energies until better data are available. At higher energies the relative sizes of the peaks are not the same. This may be due to the possibility that the high-Rydberg state population may be peaked around intermediate n values rather than high n values, which would be more analogous to ions. This could result from the higher-lying Rydberg atoms autoionizing before reaching the detector as is discussed by Van Brunt *et al.*[10] Nonetheless, good quantitative

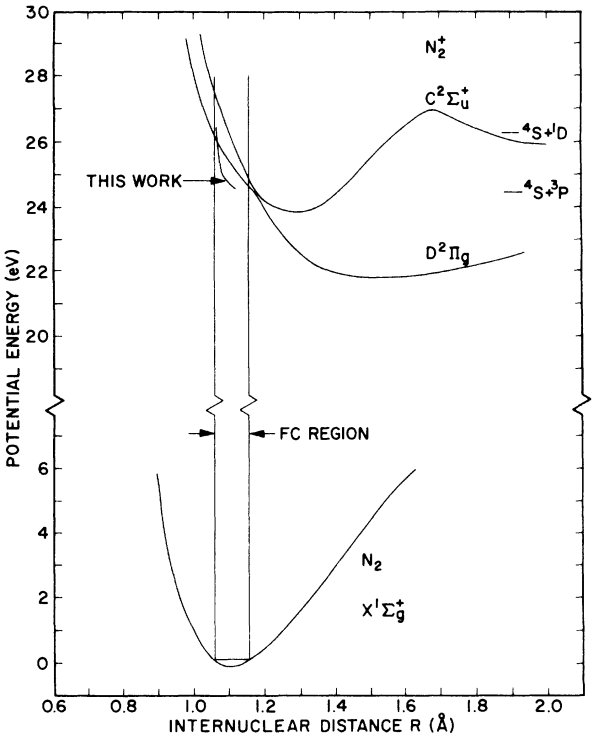

FIG. 9. Partial potential-energy diagram for N_2 and N_2^+. The Franck-Condon region is indicated for electron-impact transitions from the $v = 0$ level of the ground state of N_2. The repulsive-potential-energy curve constructed from the kinetic-energy distribution at 27.5 eV following the techniques in Sec. II C probably corresponds to more than one state. Dissociation limits for fragment atoms and ions are shown on the right. Note the break in the potential-energy scale. Potential curves for the C and D states are from Cartwright and Dunning (Ref. 31). The ground state is from Gilmore (Ref. 32).

agreement is lacking between the ion and high-Rydberg kinetic-energy spectra. This does not mean necessarily that the ion-core model is deficient, but does suggest that a more sophisticated understanding of its limitations and predictive abilities is required. In addition other competing processes such as forbidden predissociations should be considered.

D. Dissociative molecular states

Following the formulation in Sec. II C, it would be possible to construct portions of repulsive-energy curves for features 1–4 in the Franck-Condon region for molecular high-Rydberg states. We have done this for feature 1, as can be seen in Fig. 9. In general features 1–4 probably correspond to more than one process as pointed out above. Ideally, we need to unfold the kinetic-energy spectra for the various features into their component parts before constructing repulsive-potential-energy curves for single processes. The repulsive curve in Fig. 9 therefore probably corresponds to the average of 2 or more dissociative states and not just a single state.

Feature 1 correlates with the lowest ion dissociation limit. The excitation function has a sharp resonance-type behavior at threshold. Possible states that could account for this process are the $D\,^2\Pi_g$ state, the $C\,^2\Sigma_u^+$ state, and several quartet states. Smyth *et al.*[11] have considered at length the predissociation of the $C\,^2\Sigma_u^+$ state as a possible source. Wight *et al.*[28] in electron-ion coincidence experiments argues that predissociation of the $C\,^2\Sigma_u^+$ does account for the 25-eV feature they observe. The section of the potential-energy curve generated from our data (Fig. 9) lies close to the $C\,^3\Sigma_u^+$ state. On the other hand a predissociation process should have evidenced vibrational structure in the work of Smyth *et al.*, which had less thermal broadening than this work. It does appear that feature 1 corresponds to a two-electron excitation process.

Feature 2 has an excitation function which peaks around 30 eV and drops off rapidly at higher energies, characteristic of a spin-exchange process. Little is known about the analog N_2^+ state which would correlate to $N^+(^3P) + N(^2D)$ or $N^+(^3P) + N(^2P)$. Wight *et al.*[28] have tentatively associated a $F\,^2\Sigma$ state with their 29-eV feature.

Feature 3a correlates with the ion analog process where the produced fragments are $N^+(^3P)$ and $N(3s\,^4P)$. This process could correlate with the $^2\Sigma_u^+$ state of N_2^+. At higher kinetic energies, the process which dominates is the ion analog of double ionization, $N^+(^3P) + N^+(^3P)$. This double-electron-ionization process has been observed[29] in dissociative ionization experiments on N_2. The results are consistent with the excitation of the $A\,^3\Pi_g$ state of N_2^{++}.

Feature 4 occurs at higher electron-impact energies where the other fragment is uncertain. In addition to being a high-Rydberg atom or a singly ionized ion, the other fragment may be multiply ionized. As the electron-impact energy is increased in the 50–100-eV range, it would appear that many states are excited which contribute fragments with ever increasing kinetic energy. It is as if steeper potential walls were being reached by increasing the electron-impact energy. The identity of those states which account for feature 4 is unknown. It is possible that they involve multielectron excitations.

VI. SUMMARY

We have observed four principal groups of energetic nitrogen atoms in long-lived high-Rydberg states produced in electron-impact dissociation of N_2 with peak kinetic energies of 0.6, 2.4, 3.4, and 6.7 eV. We have invoked the ion-core model to explain the observed kinetic-energy spectra and excitation functions. Qualitatively, it was found satisfactory. $N(^6S_{5/2})$ was discussed as a possible dissociation product along with the high-Rydberg atoms. A cross section of $\sigma \sim 10^{-18}$ cm^2 at 180 eV was arrived at for the total production of high-Rydberg atoms assuming angular isotropy of the dissociation fragments. Where possible, dissociative molecular core-ion states of N_2^+ which correlate with ion-analog dissociative processes have been suggested as candidates responsible for the observed processes, but no unique assignments were possible.

In addition to providing information about dissociative molecular states, this work has geophysical implications. The high kinetic energies of the fragment atoms (up to 30 eV) and the large internal excitation energy (14.5 eV) of the high-Rydberg atoms may lead to chemical reactions with atmospheric gases heretofore not considered. Furthermore, the high kinetic energies contribute to the heat input in the upper atmosphere, especially under disturbed conditions such as in auroras.

Finally, the nonthermal velocities of the fragments need to be taken into account in radiative-transfer calculations of resonance radiation involving N since either the emitted line may be Doppler broadened or the ground-state atoms may have nonthermal velocities if dissociation processes are involved. This applies specifically to the $N(2p^3\,^4S^o\text{-}2p^3 3s\,^4P)$ 1200-Å transition.

*Research supported, in part, by Advanced Research Projects Agency, the Department of Defense, and was monitored by U. S. Army Research Office–Durham, under Contract No. DA-31-124-AR0-D-440, by the National Aeronautics and Space Administration (NGL39-011-030), and by the Lockheed Independent Research Program.

†Present address.

‡Present address: Department of Physics, Southern Illinois University, Carbondale, Ill. 62901.

[1]More specifically, repulsive-potential-energy curves can be constructed in the Franck-Condon region from kinetic-energy spectra deduced from the measured TOF spectra.

[2]W. C. Wells, W. L. Borst, and E. C. Zipf, Chem. Phys. Lett. 12, 288 (1971); Bull. Am. Phys. Soc. 17, 397 (1972); Trans. Am. Geophys. Union 52, 878 (1971); J. Geophys. Res. 77, 69 (1972).

[3]E. C. Zipf, E. J. Stone, M. J. Mumma, W. C. Wells and W. L. Borst, Trans. AGU 52, 308 (1971); W. C. Wells and E. C. Zipf, Trans. AGU 53, 1068 (1972); W. C. Wells and E. C. Zipf, Trans. Am. Geophys. Union 53, 459 (1972).

[4]W. C. Wells, W. L. Borst, and E. C. Zipf, *Abstracts of the Seventh International Conference on the Physics of Electronic and Atomic Collisions*, Amsterdam, 1971, edited by L. M. Branscomb *et al*. (North-Holland, Amsterdam, 1971), p. 576.

[5]W. C. Wells, W. L. Borst, and E. C. Zipf, *Electronic and Atomic Collisions, Abstracts of the Papers of the Ninth International Conference on the Physics of Electronic and Atomic Collisions* edited by J. S. Risley and R. Geballe (University of Washington, Seattle, 1975), p. 818.

[6]M. S. Feld, B. J. Feldman, and A. Javan, Phys. Rev. A 1, 257 (1973).

[7]This paper is the first in a series describing in detail our translational spectroscopic studies of metastable fragments produced by electron impact on atmospheric gases. Brief reports (Refs. 3–6) have appeared describing this work and extensive papers on oxygen [W. L. Borst and E. C. Zipf, Phys. Rev. A 4, 153 (1971)] and methane [T. G. Finn, B. L. Carnahan, W. C. Wells, and E. C. Zipf, J. Chem. Phys. 63, 1596 (1975)] have been published previously. The work by K. C. Smyth, J. A. Schiavone, and R. S. Freund [J. Chem. Phys. 59, 5225 (1973)] is very similar. This paper thus can be used as a consistency check between the two experiments.

[8]For convenience we use the term metastable here to describe any long-lived excited state including Rydberg states.

[9]S. E. Kupriyanov, Zh. Eksp. Teor. Fiz. 55, 460 (1968) [Sov. Phys.-JETP 28, 240 (1969)].

[10]R. S. Freund, J. Chem. Phys. 54, 3125 (1971); L. J. Kieffer, G. M. Lawrence, and J. M. Slater, in Ref. 4, p. 574; R. J. Van Brunt, G. M. Lawrence, L. J. Kieffer, and J. M. Slater, J. Chem. Phys. 61, 2032 (1974).

[11]Smyth, Schiavone, and Freund, Ref. 7.

[12]M. Misakian, M. J. Mumma, and J. F. Faris, J. Chem. Phys. 62, 3442 (1975).

[13]Finn, Carnahan, Wells, and Zipf, Ref. 7.

[14]H. A. Bethe and E. E. Salpeter, *Quantum Mechanics of One- and Two-Electron Atoms* (Springer, Berlin, 1957).

[15]J. N. Bardsley, Chem. Phys. Lett. 1, 229 (1967).

[16]G. Herzberg, *Spectra of Diatomic Molecules*, 2nd ed. (Van Nostrand, Princeton, N. J., 1950).

[17]W. L. Borst, Phys. Rev. 181, 257 (1969).

[18]H. D. Hagstrum, Phys. Rev. 96, 336 (1954); W. L. Borst, Rev. Sci. Instrum. 42, 1543 (1971).

[19]W. L. Borst and E. C. Zipf, Phys. Rev. A 3, 979 (1971).

[20]W. L. Borst and E. C. Zipf, Ref. 7.

[21]W. L. Borst, Rev. Sci. Instrum. 42, 1543 (1971).

[22]A. Crowe and J. W. McConkey, J. Phys. B 6, 2108 (1973).

[23]L. J. Kieffer and R. J. Van Brunt, J. Chem. Phys. 46, 2728 (1967); L. Deleanu and J. A. D. Stockdale, J. Chem. Phys. 63, 3898 (1975); R. Locht and J. Schopman, *Abstracts of the Eigthth International Conference on the Physics of Electronic and Atomic Collisions, Belgrade*, 1973, edited by B. C. Čobić and M. V. Kurepa (Institute of Physics, Belgrade, 1973), p. 424; J. T. Tate and W. W. Lozier, Phys. Rev. 39, 254 (1932); K. Kollmann, Int. J. Mass Spectrom. Ion Phys. 17, 261 (1975); R. Locht, J. Schopman, H. Wankenne, and J. Momigny, Chem. Phys. 7, 393 (1975).

[24]C. E. Fairchild, H. P. Garg, and C. E. Johnson, Phys. Rev. A 8, 796 (1973).

[25]F. R. Innes and O. Oldenberg, J. Chem. Phys. 37, 2427 (1962); R. A. Young, R. L. Sharpless, and R. Stringham, J. Chem. Phys. 40, 117 (1964); J. M. Evenson and D. S. Burch, J. Chem. Phys. 45, 2450 (1966).

[26]A. B. Prag and K. C. Clark, J. Chem. Phys. 39, 799 (1963).

[27]C. E. Johnson and H. A. Shugart, Lawrence Berkeley Laboratory Report No. 2094, 1973 (unpublished).

[28]G. R. Wight, M. J. Van der Wiel, and C. E. Brion, J. Phys. B 9, 675 (1976).

[29]H. Ehrhardt and A. Kresling, Z. Naturforsch. A 22, 2036 (1967); J. L. Franklin and M. A. Haney, *Recent Developments in Mass Spectrometry*, edited by K. Ogata and T. Hayakawa (University Park, Baltimore, 1970), p. 909.

[30]R. J. VanBrunt and L. J. Kieffer, J. Chem. Phys. 63, 3216 (1975).

[31]O. C. Cartwright and T. H. Dunning, J. Phys. B 8, L100 (1975).

[32]F. R. Gilmore, Rand Corp. Report RM-4034-PR, 1964 (unpublished).

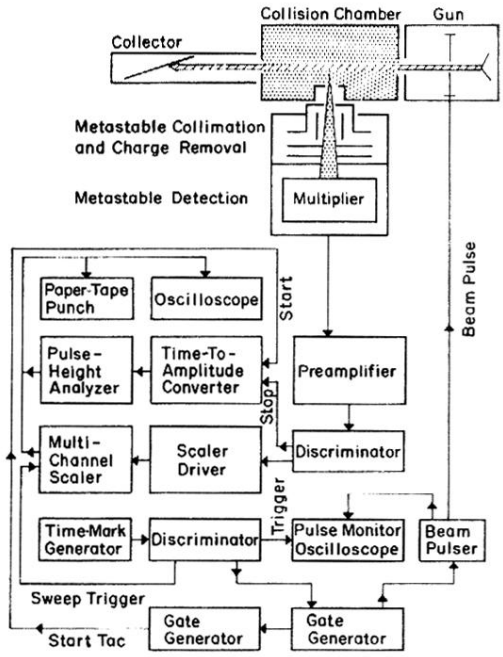

FIG. 2. Schematic diagram of the experimental apparatus used to make time-of-flight distributions. For the observations reported here the time-to-amplitude converter and the pulse-height analyzer were used.